Seismic velocity changes associated with aseismic deformations of a fault stimulated by fluid injection

D. Rivet, L. de Barros, Y. Guglielmi, F. Cappa, R. Castilla, P Henry

AGU PUBLICATIONS

Geophysical Research Letters

RESEARCH LETTER
10.1002/2016GL070410

Key Points:
- Measuring seismic velocity changes during hydraulic stimulation of a fault in shales
- Monitoring aseismic fault deformations from seismic velocity changes
- Seismic velocity changes are sensitive to both dilatant shearing and stress transfer in the fault volume

Supporting Information:
- Supporting Information S1

Correspondence to:
D. Rivet,
diane.rivet@geoazur.unice.fr

Citation:
Rivet, D., L. De Barros, Y. Guglielmi, F. Cappa, R. Castilla, and P. Henry (2016), Seismic velocity changes associated with aseismic deformations of a fault stimulated by fluid injection, *Geophys. Res. Lett.*, *43*, 9563–9572 doi:10.1002/2016GL070410.

Received 14 JAN 2016
Accepted 25 AUG 2016
Accepted article online 31 AUG 2016
Published online 28 SEP 2016

Seismic velocity changes associated with aseismic deformations of a fault stimulated by fluid injection

Diane Rivet[1], Louis De Barros[1], Yves Guglielmi[2], Frédéric Cappa[1,3], Raymi Castilla[4], and Pierre Henry[2]

[1]Université Côte d'Azur, CNRS, OCA, IRD, Géoazur, France, [2]U CEREGE, Aix-Marseille University, CNRS, IRD, Marseille, France, [3]Institut Universitaire de France, Paris, France, [4]Total, Exploration and Production, Research and Development, Pau, France

Abstract Fluid pressure plays an important role in the stability of tectonic faults. However, the in situ mechanical response of faults to fluid pressure variations is still poorly known. To address this question, we performed a fluid injection experiment in a fault zone in shales while monitoring fault movements at the injection source and seismic velocity variations from a near-distance (<10 m) monitoring network. We measured and located the *P* and *S* wave velocity perturbations in and around the fault using repetitive active sources. We observed that seismic velocity perturbations dramatically increase above 1.5 MPa of injection pressure. This is consistent with an increase of fluid flow associated with an aseismic dilatant shearing of the fault as shown by numerical modeling. We find that seismic velocity changes are sensitive to both fault opening by fluid invasion and effective stress variations and can be an efficient measurement for monitoring fluid-driven aseismic deformations of faults.

1. Introduction

Stress perturbations associated with tectonic forcing or human activities are partly accommodated along faults either by unstable, seismic slip or by stable, aseismic motion [*Avouac*, 2015]. Between those two end-member cases, a variety of seismic behaviors emerge with different signatures such as tremors and low-frequency earthquakes both observed along tectonic faults [*Peng and Gomberg*, 2010] and during fluid injection experiments [*Das and Zoback*, 2013a, 2013b; *Derode et al.*, 2015].

This spectrum of seismic signatures and slip behavior has a growing interest in clay-rich formations, which are common both in deep seismogenic zones (crustal faults and subduction zones) [*Ikari et al.*, 2009; *Faulkner et al.*, 2011] and in subsurface basins, especially in oil and gas reservoirs [*Zoback*, 2007; *Davies et al.*, 2013; *Rutqvist et al.*, 2013]. The presence of phyllosilicate minerals strongly reduces the frictional strength of faults [*Ikari et al.*, 2009; *Faulkner et al.*, 2011; *Kohli and Zoback*, 2013]. Thus, understanding seismic slip and aseismic creep in clay-rich formations is a central problem with important implications for both reservoirs engineering and tectonic faulting. However, assessing deformation and failure processes in shales is challenging. Several factors can explain this situation: (1) the failure of shales is complex due to the dependences of their mechanical properties to the mineralogy and the water content [*Ikari et al.*, 2009; *Kohli and Zoback*, 2013; *De Barros et al.*, 2016] and (2) laboratory experiments on shales are not fully representative of this complex behavior.

In order to go beyond these limitations and to better understand how clay-rich formations deform and fail in natural conditions, an in situ experiment of fluid injection-induced fault activation was performed at a few meters scale in a shale formation at a depth of 250 m in a former railroad tunnel at the Tournemire underground Experimental facility (France) [*Guglielmi et al.*, 2015]. At this site, the geological, stress, and hydromechanical settings are known [*Cornet*, 2000; *Constantin et al.*, 2004] (Figure 1a). Tournemire shale has a high content of clay minerals (39–51% of phyllosilicate) and mainly accommodates deformation through aseismic slip during hydraulic stimulation [*De Barros et al.*, 2016]. Thus, this experiment enables monitoring in situ aseismic behavior of faults developed in shales. Especially, we focus on investigating the location and origin of aseismic deformations associated with the fault rupture from seismic velocity changes using repetitive active sources (hammer shots on aluminium slab set on the tunnel walls, Figure 1b) and accelerometers in boreholes located few meters from the fault. Fluid pressure, flow rate, deformation, and seismic data were continuously recorded from several 20 m long boreholes drilled from the tunnel toward the fault zone.

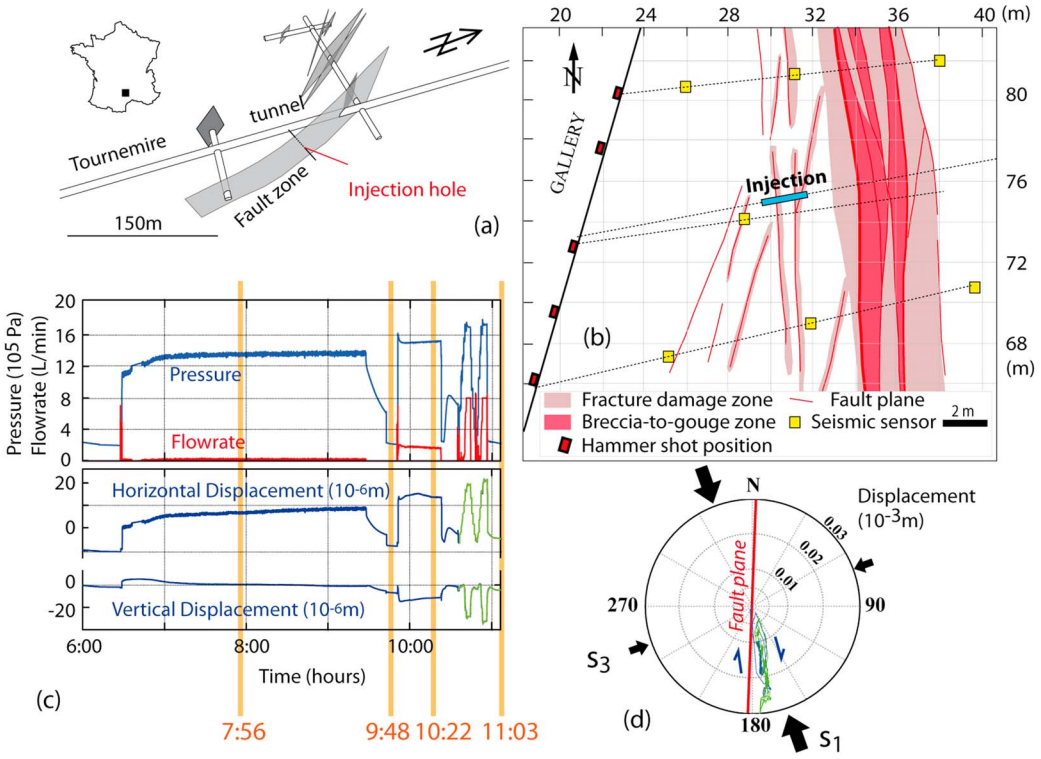

Figure 1. (a) Faults crosscutting the Tournemire underground facility and experiment location. (b) Map view of the tested fault zone together with measuring points. Black dotted lines show all the inclined boreholes with cemented accelerometers (yellow squares) and with the injection chamber (blue rectangle). Aluminium slabs anchored in the tunnel wall are shown by red squares. (c) Fluid pressure in the injection chamber and injected flow rate during the hydraulic stimulation experiment (upper graphs) and fault western compartment horizontal and vertical displacements (lower graphs). Yellow bars indicate the time of the hammer shots and active seismic imaging. (d) Horizontal displacements in polar coordinates. Concentric circles show the displacement vector variations. Red line is the main fault plane. Directions of the subhorizontal principal stresses σ_1 and σ_3 [after *Cornet*, 2000] are represented in black arrows.

Seismic velocity changes monitoring has proven its efficiency to detect slight changes (<0.1%) in the mechanical properties in fault zones. Changes in seismic velocity around active faults associated with seismic slip [e.g., *Brenguier et al.*, 2008; *Niu et al.*, 2008; *Stehly et al.*, 2015] can provide valuable information about the fault behavior. Moreover, seismic velocities are sensitive to aseismic deformation, as observed during slow slip events [*Rivet et al.*, 2011, 2014] and reservoir monitoring [*Calò et al.*, 2011; *Fiore et al.*, 2014; *Hillers et al.*, 2015]. As seismic waves are sensitive to changes in the poroelastic properties of the rock, they also allow monitoring processes like pore-pressure changes, water table variations, and stress state changes using ambient noise monitoring [*Sens-Schoenfelder and Wegler*, 2006; *Meier et al.*, 2010; *Hillers et al.*, 2014; *Rivet et al.*, 2015] or 4-D *P* waves tomography [*Calò et al.*, 2011]. In this work, we monitor aseismic deformations from seismic velocity changes in order to better constrain their mechanical origin and to understand the deformation accompanying a fluid-induced fault reactivation. Using active sources, we accurately (<0.1%) measured seismic velocity changes for direct *P* and *S* waves before, during, and after the injection. Thanks to the close multisensor monitoring, we link the seismic velocity variations near the fault with the fault displacement and the hydromechanical observations.

2. Fluid Injection Experiment

The experiment was performed at 250 m depth in a tunnel of the underground laboratory of Tournemire (France) (Figure 1a). The tunnel allows a direct access to a 250 m thick Toarcian shale formation [*Constantin et al.*, 2007] characterized by a low porosity (8–12%) and a low permeability (10^{-18} to 10^{-22} m^2) [*Bonin*, 1998; *Boisson et al.*, 2001]. Injections were performed across a ~20 m long and N0°–70-to-80°W segment of a fault of kilometer scale. The fault has a 10 m offset and is crosscutting the underground laboratory at

different places [*Constantin et al.*, 2004] (Figure 1a). Fault structure is composed of a main brecciated and foliated core zone of 20 cm to 2 m thickness and a damage zone of complex geometry made up of several subsidiary faults. Here we focus the analyses on the injection performed from a borehole in a N0°–75-to-80°W subsidiary fault (Figure 1b).

The injection was conducted with a probe that is composed of an upper and lower inflatable packer that isolates a 2.5 m long chamber allowing the forced injection of water under pressure (supporting information) [*Guglielmi et al.*, 2013]. Inside the injection chamber, a displacement sensor based on optical fibers allows measuring three-directional relative movements of the fault walls with a micrometric accuracy along a 0.5 m long base [*Guglielmi et al.*, 2015, 2013]. In addition, fluid pressure in the chamber and injection flow rate were measured.

The injection test lasted approximately 5 h and was composed of two cycles: (1) two quasi steady state pressure injections of 1.3 and 1.5 MPa, respectively, 3 and 0.5 h long, and (2) two 10 min long step-rate injections, during which the pressure is increased stepwise to pressure of 1.7 to 1.8 MPa (Figure 1c). The injected pressures were maintained below the minimum horizontal stress ($\sigma_3 \sim 2$ MPa) [*Cornet*, 2000] but raised high enough to reactivate the fault movements. The flow rate stabilized ~0.15 L/min at 1.35 MPa, reached ~1.5–2 L/min when pressure was raised to 1.5 MPa, and more than 8 L/min above 1.7 MPa. When pressure fell below 1.25 MPa, no steady flow rate was measured showing that effective stress variations strongly condition the fault permeability variation. The displacements measured in the injection chamber (Figure 1c) are strongly related to the chamber pressure variations, and they mainly display reversible variations with a residual value lower than 6×10^{-6} m. The horizontal displacement (maximum: 30×10^{-6} m) is showing a N170° dip direction in good accordance with a shear movement induced on the fault plane by the maximum horizontal stress σ_1 (Figure 1d). Above 1.4 ± 0.05 MPa, an additional N80° horizontal component occurs associated to a negative vertical movement. Thus, at this pressure level, displacements can be interpreted as normal slip-induced dilation on the N0–80 W main fault plane, leading to a fault hydraulic conductivity increase [*Guglielmi et al.*, 2015].

3. Seismic Monitoring Setup and Method

Around the injection source, we used seven three-component accelerometers cemented into three boreholes: (1) one borehole (parallel to and located at 0.5 m of the injection borehole) with a single sensor and (2) two subhorizontal boreholes (located 7.5 m south and 7.5 m north of the injection borehole, respectively) equipped with three sensors each at distances from the tunnel of about 3, 12, and 20 m, respectively. Accelerometric data were recorded continuously at a 10 kHz sampling frequency.

We use human-driven repetitive seismic sources during injection to measure seismic travel time changes due to perturbations of the elastic properties in the medium. Seismic sources are hammer shots on five aluminium slabs anchored in the tunnel wall (Figure 1b). Five different shot sequences, performed 1 month prior to the injection test, are considered as the baseline response of the medium and are used as reference seismic signals. Four series of shots were performed during the injection tests (yellow lines in Figure 1c) and are compared to the reference shots. All hammer shot signals are band-pass filtered between 200 and 1000 Hz.

4. Measurements of *P* and *S* Waves Travel Time Change

We measure travel time changes on both *P* and *S* direct waves using the Multiple Window Spectral Analysis method [*Poupinet et al.*, 1984; *Clarke et al.*, 2011] on the two horizontal components. With this method, the travel time delay between the current and the reference seismic records on windows surrounding the direct *P* and *S* waves, respectively, is measured in the frequency domain. The reliability of each travel time measurement is estimated from the coherency between the reference and current windowed signals. Based on the coherency, we estimate the weighted average of the repeated measures composed of the five reference shots and the current shot sequence that is composed of two repeated shots. In order to increase the accuracy of travel time delay measurements between two shots, we synchronize the signals recorded at all sensors based on the delay measured at the closest station to the hammer shot. Any local perturbation situated at the vicinity of the tunnel and affecting all travel times to all sensors is thus minimized.

To ensure that travel time changes measured on seismic signals are related to velocity changes in the medium, we evaluate the stability of the seismic source signal by comparing *P* and *S* wave travel time changes

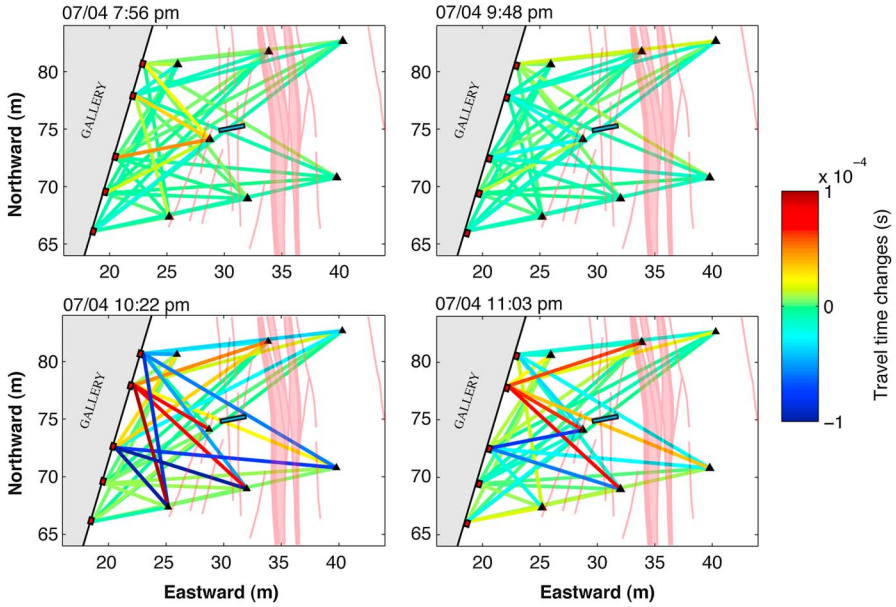

Figure 2. *P* waves travel time changes between all hammer shot positions and receivers indicated by the color of the lines linking each source and receiver for the four hammer shot sequences performed during the injection experiment.

between the hammer shots performed four days before the injection and the reference shots (Figure S3). Waveforms of the two shots performed more than 1 month apart are very similar, both for early and late arrivals. Travel time changes between the two shots for all source-receivers pairs are measured for the direct *P* waves (Figure S3b). The average absolute travel time change over all pairs is 4.8×10^{-6} s for a mean *P* wave travel time of 5.1×10^{-3} s. On average, before injection, the relative travel time change is of 0.001. Similar travel time changes are measured for the *S* waves. These measurements are estimates of the sensitivity of the method to detect seismic velocity changes in the medium, including the variations due to the injection probe which was installed at that time.

Figure 2 displays the travel time changes for the direct *P* waves for four selected hammer shot sequences performed during the injection. The travel time delays between the sources and receivers vary widely from one sequence to another. Results show that (1) at 7:56 P.M., changes are dominant around the closest station to the injection chamber, (2) at 9:48 P.M., a recovery of the travel time changes is observed, (3) at 10:22 P.M., strong travel time perturbations are measured, and (4) finally, at 11:03 P.M., a small recovery of the velocity is observed. These observations suggest that the distribution of anomalies in the medium evolved during the injection with contrasted velocity changes.

5. Localization of Seismic Velocity Changes

After processing all of the measurements of *P* and *S* wave travel time changes for all hammer source-receiver pairs, we locate the velocity anomalies using a ray-based tomographic method. The slowness model is discretized in a coarse grid composed of 6×8 square cells of 4×4 m to avoid underdetermination as the number of rays crossing the model is small.

We adapt the approach of *Barmin et al.* [2001] that is based on ray theory with a Gaussian-shaped lateral smoothing, and we estimate the 2-D distribution of the seismic velocity change anomalies in the medium by minimizing a penalty function composed of data misfit, model smoothness, and magnitude of perturbation, weighted by local path density. Finally, we use the relation linking the slowness change (Δs) and the relative velocity change ($\Delta v/v$) [*Mordret et al.*, 2014]:

$$\frac{\Delta v}{v} = -v\Delta s \tag{1}$$

P and *S* velocity models of 3500 m/s and 1900 m/s, respectively, except for cells that contain the tunnel excavation damage zone (3 m around the tunnel) where the velocity is 30% lower were estimated using calibration shots.

We assess the spatial resolution of the seismic velocity changes using the resolution matrix at all cells. Figures S4a and S4b show the spike test results for cells located at the injection point and at the main fault position, respectively. In the first case, the input perturbation is well resolved with a resolution close to the cell size (4×4 m) and a good recovery of its location and the amplitude. In the second case, the resolution decreases with a shift of the solution toward the tunnel and a poor recovery of the amplitude.

6. Time-Lapse Imaging of Velocity Changes Perturbations

From travel time changes for both *P* and *S* waves measured for the different hammer shot sequences during the injection experiment, we estimate the evolution of the spatial distribution of the velocity anomalies in the medium. Figure 3 displays both the *P* and *S* wave velocity anomalies measured before, during, and after the injections.

In details, the velocity perturbations observed for each hammer shot sequence indicate the following results:

1. In 4 April at 11:36 P.M., 4 days before the injection (Figures 3a and 3b), the relative velocity changes in the medium were lower than 0.01.
2. In 7 April at 7:56 P.M. (Figures 3c and 3d), about 1.5 h after the start of the long-duration injection with a steady state pressure of 1.3–1.35 MPa (Figure 2), an increase in *P* wave velocity around the injection chamber appeared as well as a moderate decrease of velocities in the damage zone of the tunnel wall and in the fault damage zone. Synchronously, an *S* wave velocity increase occurred close to the injection chamber in the fault damage zone immediately east of the *P* wave maximum.
3. At 9:48 P.M. (Figures 3e and 3f), both *P* and *S* waves seismic velocity recovered when no injection was performed.
4. At 10:22 P.M. (Figures 3g and 3h), the injection pressure was above 1.5 MPa. A major decrease in both the *P* and *S* wave velocities in a north-south elongated volume located southwest of the injection chamber occurred. These perturbations were surrounded by velocities increases close to the tunnel and in the main fault.
5. At 11:03 P.M. (Figures 3i and 3j), approximately 5 min after the last injection, the velocity change patterns were similar to the ones observed for the previous shots performed at 10:22 P.M., but with smaller amplitudes.
6. Finally, in 8 April at 8:12 A.M. (Figures 3k and 3l), 9 h after the end of injection, a complete *P* wave velocity recovery was observed, while slight *S* wave velocity changes still remained.

7. Seismic Velocity Variations Related to Fault Hydromechanical Response

We use 3-D hydromechanical modeling to determine the evolution of stresses during fault movements and fluid diffusion associated with injection and to compare with the evolution of seismic velocities. The 3DEC code [*Itasca Consulting Group Inc.*, 2013] is employed to represent the injected fault and four others, which are potentially connected to it by slip planes in an elastic medium ($20 \times 20 \times 20$ m) (Figure 4). Additional discussion of the model can be found in the supporting information [*Cundall*, 1988; *Witherspoon et al*., 1980; *Detournay*, 1980; *Walsh*, 1981; *Cornet*, 2000; *Dick et al*., 2013]. For simplicity, initial hydraulic and mechanical properties of all faults are considered homogeneous and identical (for more details, see *Guglielmi et al*. [2015]). The principal stresses measured in situ at the depth of the experiment ($\sigma_1 = 4.0$ MPa, $\sigma_2 = 3.8$ MPa, $\sigma_3 = 2.1$ MPa) are applied to the six boundaries of the model. The field experiment is simulated by imposing at a point source the time-dependent pressure variations measured in the injection hole. Fluid pressure gradient and viscous forces associated with fluid flow are only allowed through the faults (i.e., the surrounding medium is impervious). Model results reproduce reasonably well the measured fault displacements and injected flow rates (Figure 4). The onset of fluid diffusion is, however, more progressive in the experiments than in the numerical calculations, where it occurred in the interconnected faults when pressure was set above 1.5 MPa.

We do not attempt to make an exact match of simulated and experimental data (the observed discrepancy is related to the simple homogeneous properties assigned to the fault, the schematic four-fault geometry, and the simplified imposed injection pressure history), but rather, we try to obtain a reasonable agreement to the general evolution of both hydromechanical and seismic velocity data. Consequently, we focus on identifying the size and the location of the elastic stress variation induced by faults movements. The model shows that

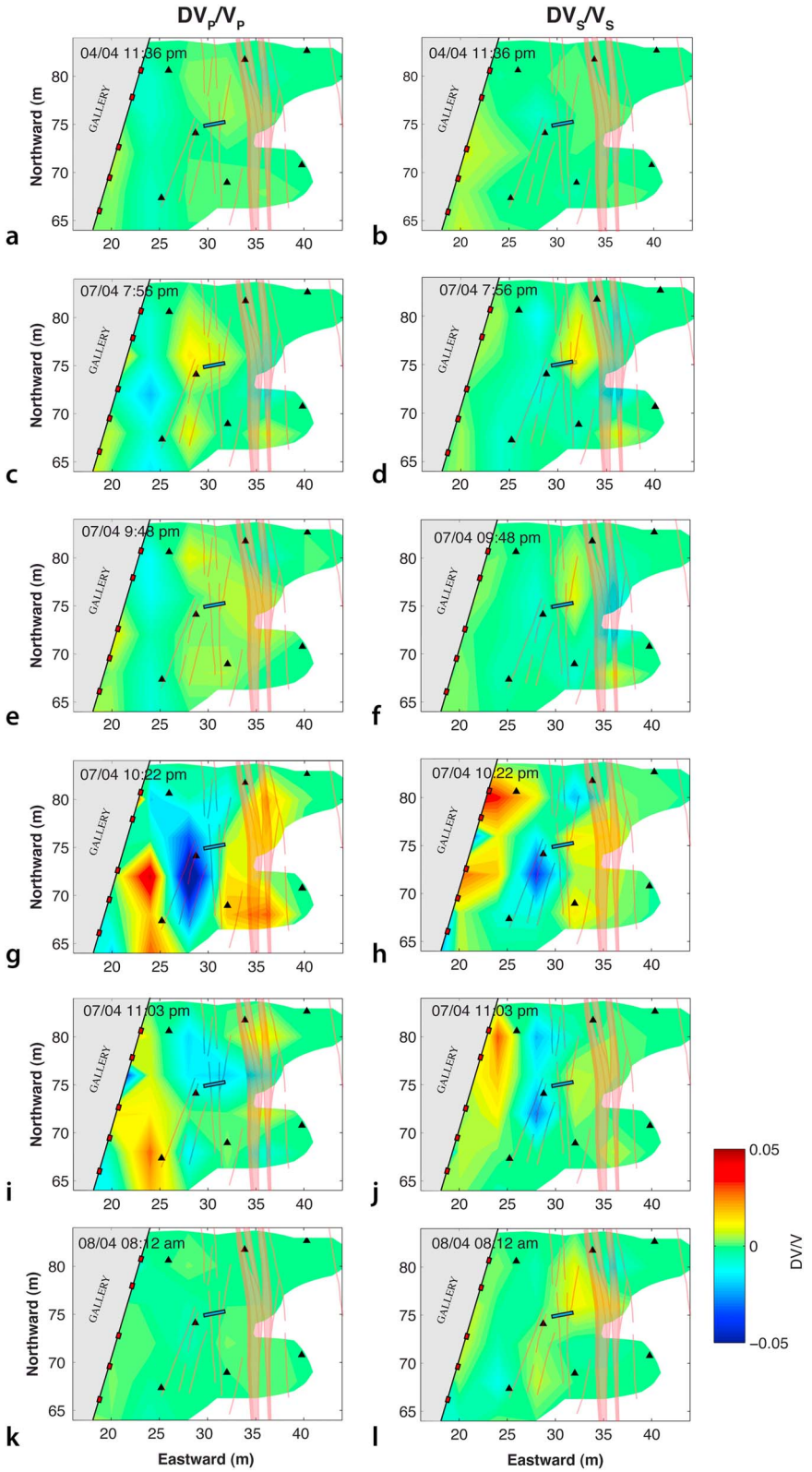

Figure 3. Distribution of *P* and *S* wave seismic velocity changes (left and right columns) (a and b) before the injection experiment 4 April at 11:36 P.M.; (c and d) during injection 7 April at 7:56 P.M.; (e and f) 9:48 P.M.; (g and h) 10:22 P.M.; (i and j) 11:03 P.M.; and (k and l) the following day at 8:12 A.M., about 9 h after the end of the injection.

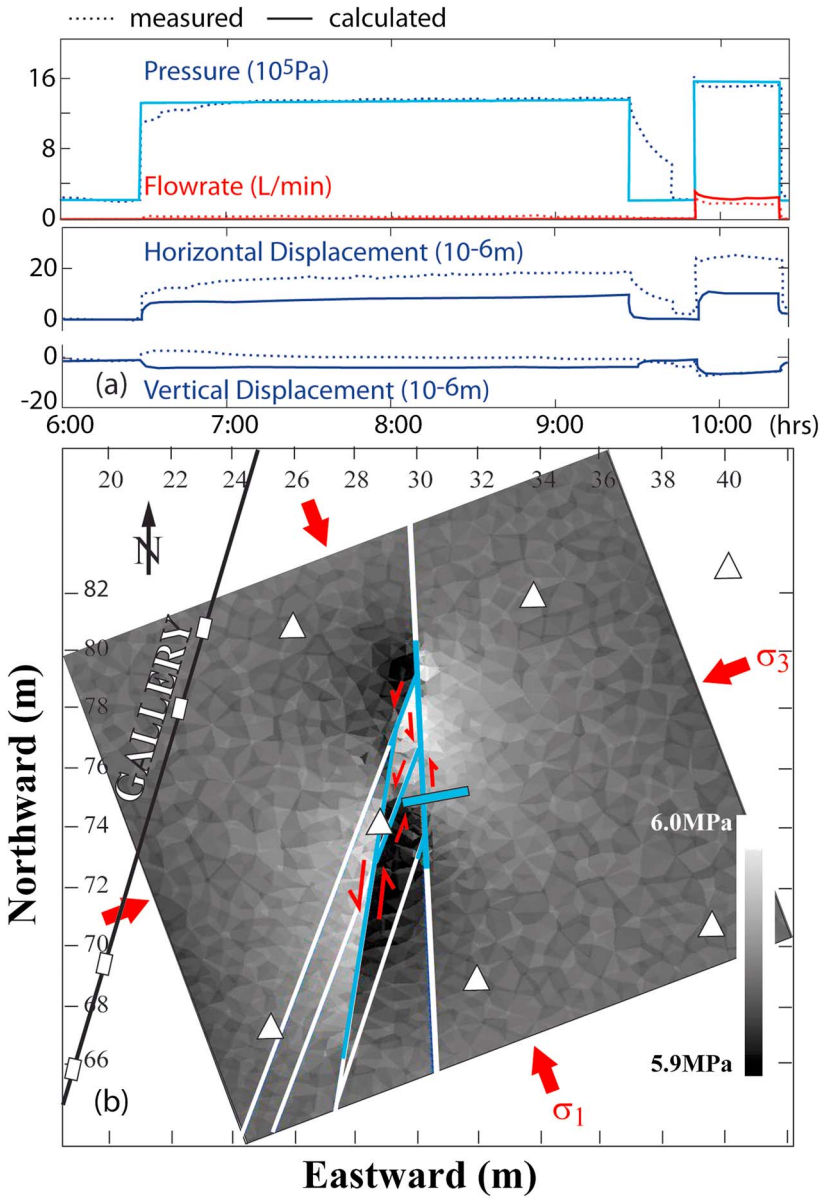

Figure 4. (a) Calculated and measured flow rate and fault movements. (b) Norm of stress in a horizontal plane located 2 m below the injection zone for an injection pressure at 1.5 MPa $\|\sigma\| = \sqrt{\sigma_{11}{}^2 + \sigma_{22}{}^2 + \sigma_{33}{}^2 + 2\times(\sigma_{12}{}^2 + \sigma_{13}{}^2 + \sigma_{23}{}^2)}$.

the strike slip reactivation of the faults produces a variation of the elastic stress within an area of decameter scale (Figure 4) for pressure above 1.5 MPa. It also reproduces the hydromechanical elastic behavior of the injected fault which explains why at the end of the experiments both the measured fault displacements and the seismic velocities almost return to initial following the drainage of the injected fluids.

Below 1.4 MPa, the flow in the fractures is small, a few 100 mL/min. However, during the first 3 h long injection phase, 12 L had flowed into the formation and leaks were observed in boreholes up to 7.5 m from the injection borehole. Fluid thus diffused in the fracture network. The displacements monitored at the injection point are, however, small (Figure 1c). The increase of *P* and *S* waves velocity of 0.01 observed around the injection chamber might be due to the elastic closing of cracks surrounding the borehole as it is commonly observed around pressurized holes [*Schmitt et al.*, 2012]. It is also possible that fluid inflow at relatively low pressure filled some initially void cracks, increasing *P* wave velocity but not *S* wave velocity, which may contribute to explain the different distributions of the *P* and *S* wave perturbations in Figures 3c and 3d. These effects are not seen in the hydromechanical model that did not represent the borehole geometry or flow below 1.5 MPa.

Above 1.5 MPa, flow occurs into faults related to stress-enhanced permeability. In the model, this is explained by the complex combination of a poroelastic normal opening and a plastic dilatant slip on the different faults [*Guglielmi et al*., 2015]. Both *P* and *S* wave velocities are affected when pressure exceeded 1.5 MPa (Figures 4g and 4h), thus corroborating that the rock poroelastic properties were perturbed during injection. The velocity drop zone close to the injection corresponds in the numerical model to the compartment bounded by the two mainly reactivated faults. A left-lateral slip is observed mainly on the western fault, which experienced a higher slip than the injected one, because it is more critically oriented toward the principal stresses. The induced stress changes, together with the openings of the fault planes and smaller cracks in their damage zones (not considered in the modeling), might be responsible for the decrease of both *P* and *S* wave velocities. The extent of the stress variation is in reasonable accordance with the extent of the velocity anomaly. Differences in the location of the anomalies may result from the coarse meshing used for the velocity tomography as well as the oversimplified mechanical model geometry that does not represent any eastern weak zone corresponding to the main fault. Around this velocity drop zone, strike slip movements on the different existing faults cause effective stress increase. Subsequent crack closure could explain the increasing velocities. After the injection ends, velocities come back to a near initial state as (1) most of the induced deformation is reversible at short time (Figures 3i and 3j) and (2) the pressure dissipates in a few hours (Figures 3k and 3l).

In the present experiment, the amplitudes of seismic velocity change perturbations are at least 10 times higher than those observed using ambient noise cross-correlation monitoring on active faults from receivers located at the surface ($\Delta v/v \sim 0.001$) [e.g., *Brenguier et al*., 2008; *Wegler et al*., 2009; *Chen et al*., 2010; *Zaccarelli et al*., 2011; *Stehly et al*., 2015; *Taira et al*., 2015]. Nevertheless, in our experiment seismic velocity changes are measured a few meters from the mechanical perturbation, with no averaging over long distances, and with small seismic wavelength, which increases the sensitivity to small seismic velocity changes as opposed to studies performed from the surface. Seismic velocity changes from the surface might therefore be an average of stronger positive and negative perturbations, as networks do not catch the full complexity of the perturbations. Recently, seismic velocity changes monitoring was performed during geothermal injections in Basel (Switzerland) [*Hillers et al*., 2015] and in Soultz-sous–Forêts (France) [*Calò et al*., 2011]. They both showed localized and contrasted velocity changes reaching 5% at the depth of the reservoirs, which is comparable with the amplitude we obtain here.

8. Conclusion

We measured *P* and *S* wave seismic velocity changes associated with the aseismic stress perturbation around a fault stimulated by fluids injection. When pressurized fluids force fault permeability to increase, a slight micrometer-scale Coulomb reactivation associated to a dominant poroelastic response causes a velocity drop of *P* and *S* waves, together with an increase of velocities outside the injection area. These perturbations relax (to less than half of peak value) within minutes after the end of injections. Velocity changes are therefore mainly sensitive to effective stress variation, associated with fault motion and fluid invasion in a complex fault network. Finally, seismic velocities are sensitive to aseismic deformation that could precede larger fault slip nucleation and accompany induced seismicity. Therefore, seismic velocity change appears as a promising complementary method to the methods commonly used to track stress changes in storage reservoirs and fault zone, even in the lack of seismic events.

Acknowledgments

This work is supported by TOTAL S.A. for the "Fluid and Fault" project (PI: Claude Gout and Raymi Castilla). The authors thank the French Institute of Radioprotection and Nuclear Safety for help and access to the IRSN Tournemire underground laboratory. We thank J. Durand, H. Caron, and Y. Zouhair (SITES) for installing and maintaining the sensors and acquisition during the experiments. All experiment data are stored in Géoazur laboratory, CNRS, University Nice Sophia-Antipolis, and are available upon request (contact louis.debarros@geoazur.unice.fr). The paper benefited from useful comments by Gregor Hillers, an anonymous referee, and Associate Editor Andrew V. Newman.

References

Avouac, J. P. (2015), From geodetic imaging of seismic and aseismic fault slip to dynamic modeling of the seismic cycle, *Annu. Rev. Earth Planet. Sci.*, *43*, 8.1–8.39, doi:10.1146/annurev-earth-060614-105302.

Barmin, M. P., M. H. Riltzwoller, and A. L. L. Levshin (2001), A fast and reliable method for surface wave tomography, *Pure Appl. Geophys.*, *158*, 1351–1375.

Boisson, J. Y., L. Bertrand, J. F. Heitz, and Y. Moreau-Le Golvan (2001), In situ laboratory investigations of fluid flow through an argillaceous formation at different scales of space and time, Tournemire tunnel, southern France, *Hydrogeol. J.*, *9*, 108–123.

Bonin, B. (1998), Deep geological disposal in argillaceous formations: Studies at the Tournemire test site, *J. Contam. Hydrol.*, *35*, 315–330.

Brenguier, F., M. Campillo, C. Hadziioannou, N. M. Shapiro, R. M. Nadeau, and E. Larose (2008), Postseismic relaxation along the San Andreas fault at Parkfield from continuous seismological observations, *Science*, *321*(5895), 1478–1481, doi:10.1126/science.1160943.

Calò, M., C. Dorbath, F. H. Cornet, and N. Cuenot (2011), Large-scale aseismic motion identified through 4-D *P*-wave tomography, *Geophys. J. Int.*, *186*(3), 1295–1314.

Chen, J. H., B. Froment, Q. Y. Liu, and M. Campillo (2010), Distribution of seismic wave speed changes associated with the 12 May 2008 Mw 7.9 Wenchuan earthquake, *Geophys. Res. Lett.*, *37*, L18302, doi:10.1029/2010GL044582.

Clarke, D., L. Zaccarelli, N. M. Shapiro, and F. Brenguier (2011), Assessment of resolution and accuracy of the Moving Window Cross Spectral technique for monitoring crustal temporal variations using ambient seismic noise, *Geophys. J. Int.*, *186*(2), 867–882.
Constantin, J., J. B. Peyaud, P. Vergély, M. Pagel, and J. Cabrera (2004), Evolution of the structural fault permeability in argillaceous rocks in a polyphased tectonic context, *Phys. Chem. Earth*, *29*, 25–41.
Constantin, J., P. Laurent, P. Vergély, and J. Cabrera (2007), Paleo-deviatoric stress magnitudes from calcite twins and related structural permeability evolution in minor fault: Example from the toarcian shale of the French Causses Basin, Aveyron, France, *Tectonophysics*, *429*, 79–97.
Cornet, F. H. (2000), Détermination du champ de contrainte au voisinage du laboratoire souterrain de Tournemire, Rapport du Laboratoire de Mécanique des Roches, Département de Sismologie, Institut de Physique du Globe de Paris, Rapport N°98 N33/0073.
Cundall, P. A. (1988), Formulation of a three-dimensional distinct element model—Part I: A scheme to detect and represent contacts in a system composed of many polyhedral blocks, *Int. J. Rock Mech. Min. Sci. Geomech. Abstr.*, *25*, 107–116.
Das, I., and M. D. Zoback (2013a), Long-period, long-duration seismic events during hydraulic stimulation of shale and tight-gas reservoirs—Part 1: Waveform characteristics, *Geophysics*, *78*(6), KS97–KS108.
Das, I., and M. Zoback (2013b), Long-period long-duration seismic events during hydraulic stimulation of shale and tight gas reservoirs—Part 2: Location and mechanisms, *Geophysics*, *78*(6), KS97–KS105.
Davies, R., G. Foulger, A. Bindley, and P. Styles (2013), Induced seismicity and hydraulic fracturing for the recovery of hydrocarbons, *Mar. Pet. Geol.*, *45*, 171–185.
De Barros, L., et al. (2016), Fault structure, stress or pressure control of the seismicity in shale? Insights from a controlled experiment of fluid-induced fault reactivation, *J. Geophys. Res. Solid Earth*, doi:10.1002/2015JB012633, in press.
Derode, B., Y. Guglielmi, L. De Barros, and F. Cappa (2015), Seismic responses to fluid pressure perturbations in a slipping fault, *Geophys. Res. Lett.*, *42*, 3197–3203, doi:10.1002/2015GL063671.
Detournay, E. (1980), Hydraulic conductivity of closed rock fracture: An experimental and analytical study. Proceedings of the 13th Canadian rock mechanics symposium.
Dick, P., A. Du Peloux de Saint Romain, E. Moreno, C. Homberg, F. Renel, A. Dauzères, C. Wittebroodt, and J. Matray (2013), Structural and petrophysical characterization of fault zones in shales: Example from the Tournemire URL (SW, France). In AGU Fall Meeting Abstracts (Vol. 1, p. 1138).
Faulkner, R., M. Mitchell, J. Behnsen, T. Hirose, and T. Shimamoto (2011), Stuck in the mud? Earthquake nucleation and propagation through accretionary forearcs, *Geophys. Res. Lett.*, *38*, L18303, doi:10.1029/2011GL048552.
Fiore, J., C. Hubans, and E. Brechet (2014), 4D seismic warping in two steps for overburden and reservoir—Example of a compacting carbonate field. In 76th EAGE Conference and Exhibition 2014.
Guglielmi, Y., F. Cappa, H. Lançon, J. B. Janowczyk, J. Rutqvist, C. F. Tsang, and J. S. Y. Wang (2013), ISRM suggested method for step-rate injection method for fracture in-situ properties (SIMFIP): Using a 3-components borehole deformation sensor, *Rock Mech. Rock Eng.*, *47*, 303–311, doi:10.1007/s00603-013-0517-1.
Guglielmi, Y., D. Elsworth, F. Cappa, P. Henry, C. Gout, P. Dick, and J. Durand (2015), In situ observations on the coupling between hydraulic diffusivity and displacements during fault reactivation in shales, *J. Geophys. Res. Solid Earth*, *120*, 7729–7748, doi:10.1002/2015JB012158.
Hillers, G., M. Campillo, and K.-F. Ma (2014), Seismic velocity variations at TCDP are controlled by MJO driven precipitation pattern and high fluid discharge properties, *Earth Planet. Sci. Lett.*, *391*, 121–127, doi:10.1016/j.epsl.2014.01.040.
Hillers, G., S. Husen, A. Obermann, T. Planès, E. Larose, and M. Campillo (2015), Noise-based monitoring and imaging of aseismic transient deformation induced by the 2006 Basel reservoir stimulation, *Geophysics*, *80*(4).
Ikari, M. J., D. M. Saffer, and C. Marone (2009), Frictional and hydrologic properties of clay-rich fault gouge, *J. Geophys. Res.*, *114*, B05409, doi:10.1029/2008JB006089.
Itasca Consulting Group, Inc. (2013), 3DEC — Three-Dimensional Distinct Element Code, Ver. 5.0., Minneapolis, Itasca, Ill.
Kohli, A. H., and M. D. Zoback (2013), Frictional properties of shale reservoir rocks, *J. Geophys. Res. Solid Earth*, *118*, 5109–5125, doi:10.1002/jgrb.50346.
Meier, U., N. M. Shapiro, and F. Brenguier (2010), Detecting seasonal variations in seismic velocities within Los Angeles basin from correlations of ambient seismic noise, *Geophys. J. Int.*, *181*(2), 985–996, doi:10.1111/j.1365-246X.2010.04550.x.
Mordret, A., N. M. Shapiro, and S. Singh (2014), Seismic noise-based time-lapse monitoring of the Valhall overburden, *Geophys. Res. Lett.*, *41*, 4945–4952, doi:10.1002/2014GL060602.
Niu, F., P. G. Silver, T. M. Daley, X. Cheng and E. L. Majer (2008), Preseismic velocity changes observed from active source monitoring at the Parkfield SAFOD drill site, *Nature*, *454*(7201), 204–208.
Peng, Z., and J. Gomberg (2010), An integrated perspective of the continuum between earthquakes and slow-slip phenomena, *Nat. Geosci.*, *3*, 599–607.
Poupinet, G., W. L. Ellsworth, and J. Frechet (1984), Monitoring velocity variations in the crust using earthquake doublets—An application to the Calaveras Fault, California, *J. Geophys. Res.*, *89*(B7), 5719–5731.
Rivet, D., M. Campillo, N. M. Shapiro, V. Cruz-Atienza, M. Radiguet, N. Cotte, and V. Kostoglodov (2011), Seismic evidence of nonlinear crustal deformation during a large slow slip event in Mexico, *Geophys. Res. Lett.*, *38*, L08308, doi:10.1029/2011GL047151.
Rivet, D., et al. (2014), Seismic velocity changes, strain rate and non-volcanic tremors during the 2009–2010 slow slip event in Guerrero, Mexico, *Geophys. J. Int.*, *196*(1), 447–460.
Rivet, D., F. Brenguier, and F. Cappa (2015), Improved detection of preeruptive seismic velocity drops at the Piton de La Fournaise volcano, *Geophys. Res. Lett.*, *42*, 6332–6339, doi:10.1002/2015GL064835.
Rutqvist, J., A. P. Rinaldi, F. Cappa, and G. J. Moridis (2013), Modeling of fault reactivation and induced seismicity during hydraulic fracturing of shale-gas reservoirs, *J. Petrol. Sci. Eng.*, *107*, 31–44.
Schmitt, D. R., C. A. Currie, and L. Zhang (2012), Crustal stress determination from boreholes and rock cores: Fundamental principles, *Tectonophysics*, *580*, 1–26.
Sens-Schoenfelder, C., and U. Wegler (2006), Passive image interferometry and seasonal variations at Merapi volcano, Indonesia, *Geophys. Res. Lett.*, *33*, L21302, doi:10.1029/2006GL027797.
Stehly, L., B. Froment, M. Campillo, Q. Y. Liu, and J. H. Chen (2015), Monitoring seismic wave velocity changes associated with the Mw 7.9 Wenchuan earthquake: Increasing the temporal resolution using curvelet filters, *Geophys. J. Int.*, *201*(3), 1939–1949.
Taira, T. A., F. Brenguier, and Q. Kong (2015), Ambient noise-based monitoring of seismic velocity changes associated with the 2014 Mw 6.0 South Napa earthquake, *Geophys. Res. Lett.*, *42*, 6997–7004, doi:10.1002/2015GL065308.
Walsh, J. B. (1981), Effect of pore pressure and confining pressure on fracture permeability, *Int. J. Rock Mech. Mining Sci. Geomech. Abstr.*, *18*(5), 429–435.

Wegler, U., H. Nakahara, C. Sens-Schoënfelder, M. Korn, and K. Shiomi (2009), Sudden drop of seismic velocity after the 2004 M_w 6.6 mid-Niigata earthquake, Japan, observed with Passive Image Interferometry, *J. Geophys. Res.*, *114*, B06305, doi:10.1029/2008JB005869.

Witherspoon, P. F., J. S. Y. Wang, K. Iwai, and J. E. Gale (1980), Validity of cubic law for fluid flow in a deformable rock fracture, *Water Resour. Res.*, *16*(6), 1016–1024, doi:10.1029/WR016i006p01016.

Zaccarelli, L., N. M. Shapiro, L. Faenza, G. Soldati, and A. Michelini (2011), Variations of crustal elastic properties during the 2009 L'Aquila earthquake inferred from cross-correlations of ambient seismic noise, *Geophys. Res. Lett.*, *38*, L24304, doi:10.1029/2011GL049750.

Zoback, M. D. (2007), *Reservoir Geomechanics*, pp. 459, Cambridge Univ. Press.